# A Consideration of Vibration Suppression Control of Parallel Shaft e-Axle Using Phase Stabilization Control Based on System Identification

| | | | |
|---|---|---|---|
| Michi Oda[*,**a)] | Member, | Sakahisa Nagai[*] | Member |
| Hiroshi Fujimoto[*] | Senior Member, | Hidemasa Fujita[***] | Non-member |
| Kota Yamamoto[***] | Non-member, | Tohru Urano[***] | Non-member |
| Koji Sato[**] | Non-member, | Kana Mizoguchi[**] | Non-member |
| Naoki Takizawa [**] | Non-member | | |

Recently, vehicles using an e-Axle unit are increasing because of vehicle's electrification. The e-Axle unit helps vehicle design and cost down. However, the riding comfort is worsened by mechanical vibration caused by drive shafts and motor mounts. In this paper, we did the system identification examinations of the actual vehicle using an e-Axle unit and designed the phase stabilization controller based on the identification results for vibration suppression. From the results, we found that the system could not be assumed as a simple two-inertia model. Therefore, the transfer functions were derived by increasing the order. The driving force controller is constructed using the transfer functions. The performance was confirmed by the step response. As a result, the designed controller can suppress the vibration. Therefore, the process of the general controller design based on the system identification results in servo motors can be applied to the vehicle control system.

**Keywords:** e-Axle, electric vehicle, vibration suppression, driving force control, phase stabilization, speed control

## 1. Introduction

Electric vehicles (EVs) are superior to engine vehicles in term of both environment-friendliness and torque control. There has been a lot of research regarding driving motion control of EVs. The torque response of EVs is about one hundred times faster than engine vehicle's torque response [1]. Therefore, they can quickly follow the reference signals such as driving force and speed by controlling the driving and regenerative braking torque. In addition, an electric motor's construction is simpler than a fuel engine. An e-Axle unit, combining a motor, an inverter, and gears, makes the driving system compact, lightweight, and low-cost [2]. A lot of research about e-Axles [3] [4] holds the potential to increase the popularity of EVs.

Lately, driving control techniques utilizing the fast torque control in EVs are studied actively. The energy efficient driving techniques using motor models, signals' information and driving logs are also studied to enhance the EVs' capability to drive long distances [5]. However, the abrupt torque fluctuations aimed at enhancing driving efficiency can lead to vibra-

tions in the vehicle body. In the case of engine vehicles, the vibration is suppressed by passive mechanical parts such as mount bushes [6], suspensions, and a notch filter applied to the engine torque command. On the other hand, EVs can actively suppress the vibration by outputting positive and negative torque with quick and accurate response. Currently, some research using experimental vehicles and two-inatia model are studied for the vibration suppression of EVs [7] [8]. This paper aims for the suppression of the vibration due to the inclusions of elastic components such as driving shafts and mounting bushes to improve the riding comfort by utilizing the high torque response of an e-Axle.

It is well known that experiments using a test bench are very useful because the evaluation of the controller can be easily conducted [9] [10]. The experiments can show the wide range frequency characteristics and be used effectively for EVs. In this paper, the target vehicle is a Plug-In Hybrid Electric Vehicle (PHEV) OUTLANDER produced by MITSUBISHI MOTORS CORPORATION. The test bench including the vehicle is constructed as shown in Fig. 1. Four dynamometers are connected to the driving shaft ends and output the load torque. The controller target in this paper is the vibration suppression in the rear unit. The controller is implemented in the Rear Motor Control Unit (RMCU) without the change of the mechanical parts used in the actual vehicle. The main controller is the Driving Force Control (DFC) system using a Wheel Speed Control (WSC) and Driving Force Observer (DFO) [11]. The DFC system is robust against the slip rate changes. There is much research on traction control using the DFC system [12] [13].

Fig. 1.    The plant with test bench.



Cross member
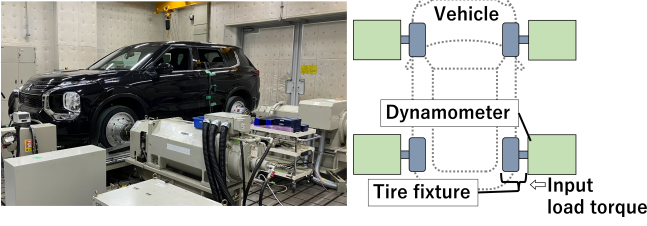e-Axle unit case
Drive motor
Reduction gear
Drive shaft
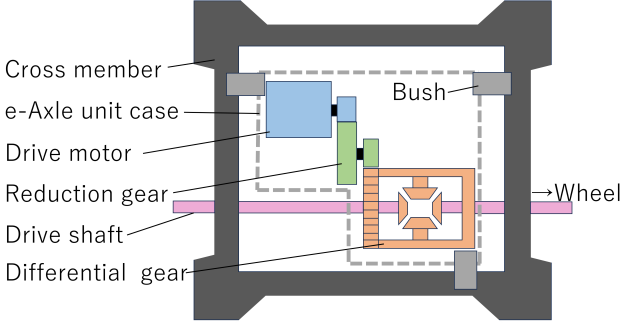Differential gear
Bush
→Wheel

Fig. 2.    The configuration of the driving unit.

In the DFC system, the vibration suppression is done using the DFC feedforward (FF) controller and WSC. The DFC FF controller is designed based on the system identification result. The WSC is a phase stabilization controller utilizing a PI controller and a phase lead compensator. The vibration suppression performance by the WSC is evaluated using Nyquist plot and sensitivity function. Our initial examination involves considering the case with a slip rate of 0. The effectiveness of the controller is assessed through step response experiments. The test bench is utilized for both the system identification experiments and step response experiments. The proposed phase stabilization controller's efficacy is evaluated by comparing it with the gain stabilization controller.

This paper is organized as follows: Section 2 describes the plant, Section 3 describes the control system, Section 4 describes the experiments, and Section 5 describes the conclusion.

## 2.  Plant Components

In this section, the plant components are described. The photograph of the plant is shown in Fig. 1. The configuration diagram of the driving unit utilized for the vehicle is shown in Fig. 2. The driving unit is composed of the parallel shaft e-Axle, drive shafts, and a cross member. The parallel shaft e-Axle includes an inverter, a driving motor, a reduction gear, and a differential gear. The e-Axle is mounted on the cross member by three bushes. The left and right drive shafts are connected to each of the two differential gear outputs. This paper focuses on the suppression of the vibration caused by the torsional stiffness of the drive shafts. The program of the DFC system including the vibration suppression is implemented in the RMCU without changes in the mechanical parts.

## 3.  Control system

In this section, the controller utilizing the DFC system with the vibration suppression is described. The block diagram of

the control system is shown in Fig. 3. The controller is composed of the DFC, the WSC, and the DFO. Here, $r$ is the wheel radius, $F_d$ is the driving force, $T^*_{m(DFC)}$ is the reference signal of the motor torque by the DFC, $K_{i(DFC)}$ is the integral gain of the DFC, $y$ is the parameter representing slip rate which is derived by the vehicle velocity and the wheel velocity [11], $V$ is the vehicle velocity, $\omega_l$ is the wheel angular velocity, $\omega_m$ is the motor angular velocity, $T$ and $\alpha$ are the parameters designing the phase lead compensator, $K_p$ is the proportional gain, $K_i$ is the integral gain and $T^*_{m(WSC)}$ is the reference signal of the motor torque by the WSC. $*$ indicates reference value and $\hat{}$ indicates estimated value. The three controllers are described in the following subsections.

**3.1  Driving Force Controller (DFC)**    This subsection describes the DFC [11]. The blue area in Fig. 3 shows the DFC which consists of a FF controller and a feedback (FB) controller. In the experiments, the vehicle velocity is estimated by the Real Car-Simulation bench (RC-S) measurement system. The estimated vehicle velocity $\widehat{V}$ is used as vehicle velocity $V$ because the plant is fixed to the test bench. The details of the RC-S measurement system is described in Section 4. The integral control is used in the DFC FB control. The reference value of the vehicle velocity $V^*$ is derived from equation (1).

$$V^* = \begin{cases} \widehat{V} + y\widehat{V} & (\widehat{V} \geqq \sigma) \\ \widehat{V} + y\sigma & (\widehat{V} < \sigma) \end{cases} \tag{1}$$

Here, $\sigma$ is the small positive value which is defined to suppress the slip rate. The reference value of the wheel angular velocity $\omega_l^*$ is derived from equation (2).

$$\omega_l^* = \frac{V^*}{r} \tag{2}$$

The DFC FF $G_{FF}(s)$ is derived by the inverse system of the transfer function from the motor torque $T_m$ to the torsional torque $T_s$. The tuning parameters of the DFC are the integral gain $K_{i(DFC)}$ and the time constant of the DFC FF $\tau_2$. These parameters are experimentally adjusted to values that provide the vibration suppression from the step response results.

**3.2  Wheel speed controller (WSC)**    This subsection describes the WSC. The red area in Fig. 3 shows the WSC. There are a FF filter $G_{(WSC)}(s)$, a PI controller, and a phase lead compensator in the WSC. Although the available parameters for the controller in the actual vehicle are the motor angular velocity $\omega_m$ and the estimated vehicle velocity $\hat{V}$, the wheel angular velocity $\omega_l$ cannot be sensed and used in the controller. Therefore, the FB parameter is the motor angular velocity. The WSC needs the FB filter $G_{(WSC)}(s)$ which transfers the reference signal of the wheel angular velocity $\omega_l^*$ calculated by the DFC FB into the reference signal of the motor angular velocity $\omega_m^*$. $G_{(WSC)}(s)$ is derived from equation (3).

$$G_{(WSC)}(s) = \frac{\omega_m(s)}{\omega_l(s)} = \frac{\omega_m(s)}{T^*_m(s)} \bigg/ \frac{\omega_l(s)}{T^*_m(s)} \tag{3}$$

System identification examinations are conducted to derive the two transfer functions from the motor torque $T^*_m$ to the wheel angular velocity $\omega_l$ and the motor angular velocity $\omega_m$.

A PI controller is used for the motor angular velocity controller. The proportional gain $K_P$ and the integral gain $K_I$
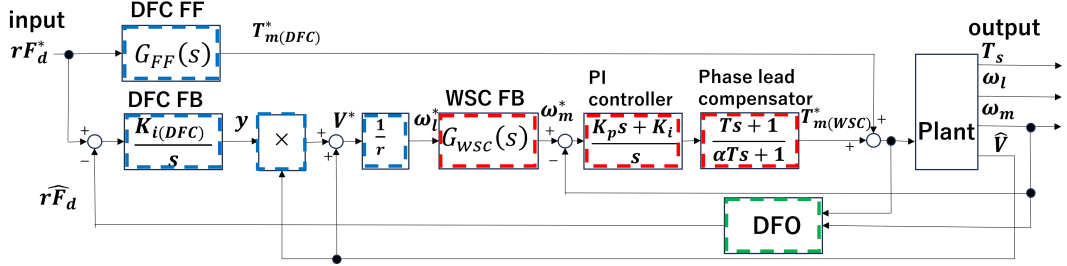
Fig. 3. The block diagram of the controller.

are derived from equations (4)(5) which are calculated using the pole assignment design considering the plant as a rigid model.

$$K_p = -2(J_1/N^2 + J_m)p \quad (4)$$

$$K_i = (J_1/N^2 + J_m)p^2 \quad (5)$$

Here, $J_1$ is the load inertia including the wheel inertia and the vehicle mass, $J_m$ is the motor inertia, $N$ is the reduction gear ratio, and $p$ is pole. The pole $p$ is adjusted to the value that provides the vibration suppression from the step response results.

In addition, a phase lead compensator is used as the phase stabilization. The parameters $\alpha$ and $T$ are derived by equations (6)(7).

$$\alpha = \frac{1 - \sin(P_h)}{1 + \sin(P_h)} \quad (6)$$

$$T = \frac{1}{2\pi \sqrt{\alpha} f_{ph}} \quad (7)$$

Here, $P_h$ is the phase lead amount and $f_{ph}$ is the phase lead frequency. The parameters of the phase lead compensator is designed using the Nyquist plot so that the phase at the resonant frequency is stabilized. One of the advantages of the phase stabilization is that the phase at low frequency does not delay.

On the other hand, a notch filter is designed as gain stabilization for comparison with the proposed phase stabilization controller. The transfer function $G_n$ is described in equation (8).

$$G_n = \frac{s^2 + 4\pi f_n \zeta ds + (2\pi f_n)^2}{s^2 + 4\pi f_n \zeta s + (2\pi f_n)^2} \quad (8)$$

Here, the notch center frequency $f_n$ is set to 10.6 Hz, the notch width $\zeta$ is set to 2, and the damping constant $d$ is set to 0.08. The notch filter suppresses the gain at the resonant frequency and is applied in the FB controller of the WSC instead of the phase lead compensator.

**3.3 Driving force observer(DFO)** This subsection describes the DFO in Fig. 3. The block diagram of the DFO is shown in Fig. 4. Here, $T_m$ is the motor torque, $\tau_{DFO}$ is the time constant of the low pass filter. Assuming that the running resistance is sufficiently small, the vehicle's kinetic model is expressed in equation (9) using the one-wheel model of Fig. 5.

$$J_1 \dot{\omega}_1 = T_s - rF_d \quad (9)$$

Here, $T_s$ is torsional torque. From equation (9), the driving torque $rF_d$ is calculated in equation (10).
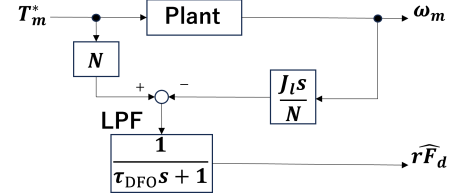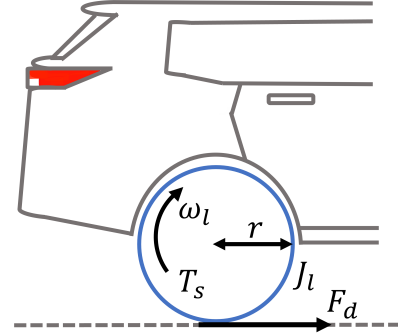


Fig. 4. The block diagram of the DFO.



Fig. 5. Driving force model.

$$rF_d = T_s - J_1 \dot{\omega}_1 \quad (10)$$

In the frequency range below the resonant frequency, the torsional torque $T_s$ and the wheel angular velocity $\omega_1$ can be regarded as in equations (11)(12) using the motor torque $T_m$ and the motor angular velocity $\omega_m$.

$$\widehat{T}_s = T_m N \quad (11)$$

$$\widehat{\omega}_1 = \omega_m/N \quad (12)$$

From equations (10)-(12), the driving torque $rF_d$ is calculated in equation (13).

$$\widehat{rF}_d = T_m N - J_1 \dot{\omega}_m/N \quad (13)$$

From equation (13), driving torque $\widehat{rF}_d$ is estimated from the motor angular velocity $\omega_m$. A low pass filter is applied to the estimated value.

## 4. Experiments

This section describes the experiments of the system identification examinations for designing the filters and the step response experiments for the evaluation of the vibration suppression effects. The RC-S system (Ono Sokki Co., Ltd.) [14] is utilized for these experiments. The RC-S system uses low-inertia dynamometers which can achieve fast torque response and simulate the running resistance on wheels accurately.
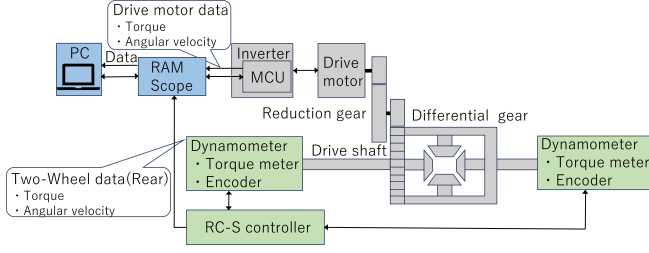
The experimental environment is shown in Fig. 6. The

Fig. 6. The configuration diagram of the experiment.



Fig. 7. The transfer functions of measurement result and fitted curve($\omega_{\mathrm{m}}/T_{\mathrm{m}}^*$).



Fig. 8. The transfer functions of measurement result and fitted curve($\omega_{\mathrm{l}}/T_{\mathrm{m}}^*$).

plant is shown in the gray parts, the RC-S system is shown in the green parts, and the data recording devices are shown in the blue parts. The ends of the right and left drive shafts are connected to the dynamometers of the RC-S system. When torque is applied to the e-Axle's motor, the dynamometers simulate the wheel behavior based on the vehicle motion model. The motor torque and angular velocity are measured by the e-Axle unit and recorded through RAMScope (DTS INSIGHT Corporation). The torsional torque and the wheel angular velocity are measured by the sensors which are connected between the plant and dynamometers and recorded through the control panel of the RC-S system and RAMScope.

**4.1 System identification** This subsection describes the system identification examination. The transfer characteristics are measured for designing the DFC FF $G_{\mathrm{FF}}(s)$ and the WSC FB $G_{\mathrm{WSC}}(s)$ used in the DFC system. Here, the input signal is the motor torque, and the output signals are the motor angular velocity, the wheel angular velocity, and the torsional torque. These transfer functions $\omega_{\mathrm{m}}(s)/T_{\mathrm{m}}^*(s)$, $\omega_{\mathrm{l}}(s)/T_{\mathrm{m}}^*(s)$, $T_{\mathrm{s}}(s)/T_{\mathrm{m}}^*(s)$ are obtained by fitting the results of the transfer characteristics, so that the DFC FF $G_{\mathrm{FF}}(s)$ and the WSC FB $G_{\mathrm{WSC}}(s)$ in Fig. 3 are designed. The input signal is a chirp sine wave of 0.05 Hz～30 Hz to obtain the frequency characteristics of the low frequency range where the riding comfort is well discussed [15].

The measurement results and the fitted transfer functions of $\omega_{\mathrm{m}}(s)/T_{\mathrm{m}}^*(s)$, $\omega_{\mathrm{l}}(s)/T_{\mathrm{m}}^*(s)$, $T_{\mathrm{s}}(s)/T_{\mathrm{m}}^*(s)$ are shown in Fig. 7, Fig. 8, and Fig. 9. The blue dots are the measurement results of the frequency-domain transfer characteristics. In these results, there is a resonance at 10.6 Hz because of the torsional stiffness of the drive shafts. From the measured characteristics, it is clear that the kinetic model of the plant cannot be represented by a two-inertia model because an anti-resonance is observed in the results of $\omega_{\mathrm{l}}(s)/T_{\mathrm{m}}^*(s)$ in Fig. 8. Therefore, the number of order of the transfer functions is increased. The transfer functions are derived as in equations (14)(15)(16). These transfer functions are shown by the red lines in the figures. The phase lag between the measurement result and the fitted curve is caused by the time delay.

$$\frac{\omega_{\mathrm{m}}(s)}{T_{\mathrm{m}}^*(s)} = \frac{46.35s^4 + 2604s^3 + 8.768 \times 10^4 s^2 + 5.302 \times 10^4 s + 8.547 \times 10^5}{s^5 + 71.59s^4 + 6376s^3 + 2.399 \times 10^5 s^2 + 3.867 \times 10^6 s} \times e^{-0.008s} \quad (14)$$

$$\frac{\omega_{\mathrm{l}}(s)}{T_{\mathrm{m}}^*(s)} = \frac{45.99s^3 + 5664s^2 + 6839s + 1.049 \times 10^5}{s^5 + 71.59s^4 + 6376s^3 + 2.399 \times 10^5 s^2 + 3.867 \times 10^6 s} \times e^{-0.008s} \quad (15)$$

$$\frac{T_{\mathrm{s}}(s)}{T_{\mathrm{m}}^*(s)} = \frac{212.7s^4 + 5.23 \times 10^4 s^3 + 1.947 \times 10^6 s^2 + 3.14 \times 10^7 s}{s^5 + 71.59s^4 + 6376s^3 + 2.399 \times 10^5 s^2 + 3.867 \times 10^6 s} \times e^{-0.008s} \quad (16)$$
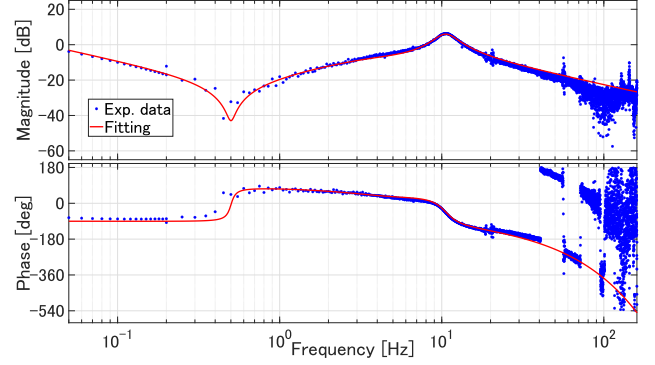
From equations (14)(15), the WSC FB $G_{\mathrm{(WSC)}}(s)$ is designed
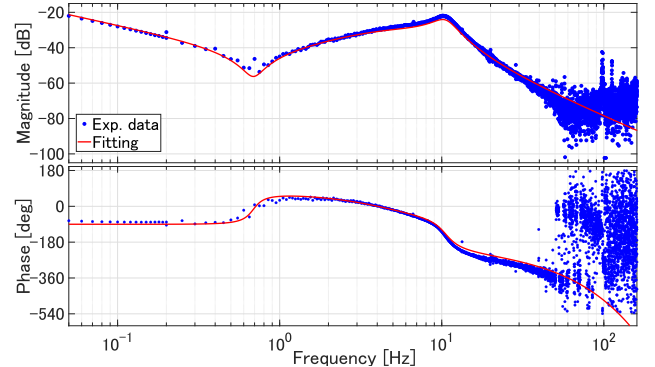
as equation (17).

$$G_{\mathrm{(WSC)}}(s) = \frac{\omega_{\mathrm{m}}(s)}{T_{\mathrm{m}}^*(s)} / \frac{\omega_{\mathrm{l}}(s)}{T_{\mathrm{m}}^*(s)} \times \frac{1}{(\tau_1 s + 1)} \quad (17)$$

Considering the WSC FB filter, the order of the denominator is smaller than the order of the numerator. Therefore, a first-order low pass filter $\frac{1}{(\tau_1 s+1)}$ is added so that the WSC FB filter becomes a proper transfer function. From equation (16), the DFC FF $G_{\mathrm{(FF)}}(s)$ is designed as equation (18).

$$G_{\mathrm{(FF)}}(s) = \frac{T_{\mathrm{m}}^*(s)}{T_{\mathrm{s}}(s)} \times \frac{1}{(\tau_2 s + 1)} \quad (18)$$

As the same in the WSC FB Filter, a first-order low pass filter $\frac{1}{(\tau_2 s+1)}$ is added so that the DFC FF filter becomes a proper transfer function. Here, the time delay is not included in order to avoid complication of the controller calculation.

**4.2 Design of the phase stabilization controller in the WSC** This subsection describes the design of the phase stabilization controller in the WSC. From the step response experiments described in the next section, the pole $p$ is set at 0.3 rad/s to obtain the vibration suppression effects. From equations (4)(5), $K_{\mathrm{P}}$ is calculated as 2.6775 and $K_{\mathrm{I}}$ is calculated as 0.4016.

The phase stabilization controller is designed using Nyquist diagram, so that the phase of the resonance is close to 0 deg [16]. Several phase lead compensators are compared. Fig. 10 shows the relationship between the phase at the resonance and the sensitivity function peak. There is a trade-off between the phase at the resonance and disturbance suppression. In this paper, the phase lead amount $P$h and the phase

Fig. 9. The transfer functions of measurement result and fitted curve($T_s/T_m^*$).



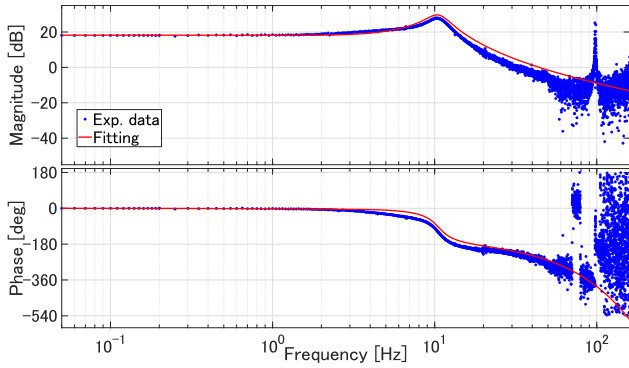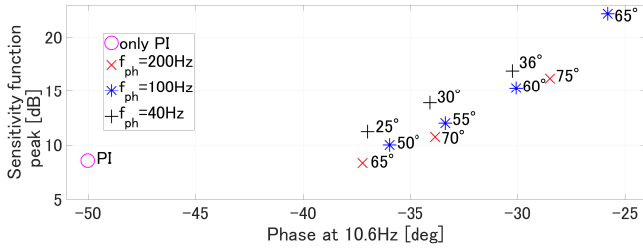Fig. 10. The relationship between the phase at the resonance and the sensitivity function peak.



Fig. 11. Nyquist plots (Left:fitted model, Right:measured data).



Fig. 12. Sensitivity function.

Table 1. Experiment parameters.

| Parameter | Value |
|-----------|-------|
| $K_I$ | 0.001 |
| $\tau_1$ | 0.05 |
| $\tau_2$ | 0.05 |
| $\tau_{DFO}$ | 1/125.6 |
| $p$ | 0.3 |

lead frequency $f_{ph}$ are set to 36 deg and 40 Hz respectively. Fig. 11 shows the Nyquist diagram of the WSC control's open loop based on the result of the system identification examination in Fig. 7 and indicates the stability of the WSC control. The blue line shows the Nyquist diagram of the plant without the controller. The red line shows the case of the plant with PI control. The black line shows the case of phase stabilization (PI+phase lead compensator). The green line shows the case of gain stabilization (PI+notch filter). These small circles show several points at 10.6 Hz. The pink dotted line is the circle of radius 1 centered at (0, 0), indicating gain 0 dB. The pink line is the circle of the sensitivity function centered at (-1, 0). If Nyquist plot is out of the circle of the sensitivity function, the disturbance is suppressed at the frequency. If Nyquist plot is in the circle, the disturbance is amplified at the frequency. Fig. 12 shows the sensitivity function. The sensitivity function is the inverse of the distance to (-1, 0) in the Nyquist diagram and indicates the disturbance suppression characteristics. According to Fig. 11 and Fig. 12, the gain stabilization can suppress the gain of the resonant frequency. However, the gain stabilization cannot suppress the influence of the disturbance such as slippage. In the case of the phase stabilization, the sensitivity around 30 Hz not relating the driving shaft resonance is increased. However, the disturbance around the resonant frequency of 10.6 Hz relating riding comfort can be suppressed.

**4.3 Measurement of step response** This section describes the step response experiments. The vibration suppression effects are evaluated by the step response results. In this paper, the slip rate in the RC-S system is set to 0. Therefore, the rotation and the torque are transmitted without loss. The reference of the driving force $rF_d^*$ is changed from 0 Nm to 326 Nm. The initial vehicle velocity is set at 0 km/h and 20 km/h.
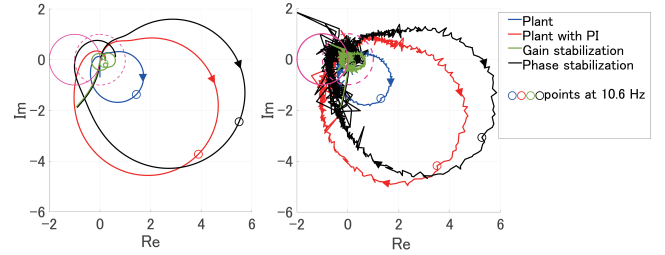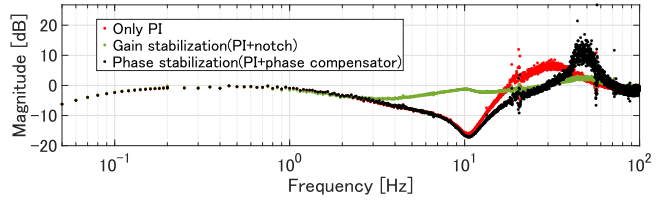
The parameters of the controller described in Section 2 greatly affect the vibration suppression effects of the controller. The parameters are adjusted based on the step response to obtain the vibration suppression effects, as shown in Table 1.

Fig. 13, Fig. 14, and Fig. 15 indicate the step response of the motor angular velocity and the FFT results from 4 s to 20 s which is in the steady state. Blue and green lines are results of the gain stabilization. Orange and purple lines are results of the phase stabilization. In the cases of blue and orange lines, the initial vehicle velocity is 0 km/h. In the cases of green and purple lines, the initial vehicle velocity is 20 km/h. These results indicate that there is disturbance depending on the vehicle velocity. The phase stabilization can suppress the disturbance in a range of 8 Hz to 20 Hz around the resonant frequency of 10.6 Hz more than the gain stabilization. It can be explained by the sensitivity functions of Fig. 12.

Fig. 16 indicates the step response of the torsional torque. In the case of the initial velocity of 0 km/h, the overshoot with the gain stabilization is 534 Nm. With the phase stabilization, torsional torque quickly converges to the constant torque. In the case of the initial velocity of 20 km/h, the overshoot with the gain stabilization is 723 Nm. The overshoot with the phase stabilization is 564 Nm and reduced. These results reveal that the vibration at startup and acceleration can be reduced by the phase stabilization.

## 5. Conclusion

This paper aims to develop the vibration suppression of the actual vehicle including elastic components for improvement of the riding comfort. The actual vehicle OUTLANDER is tested on the RC-S test bench. The controller using DFC,

WSC, and DFO is applied to the RMCU. The control filters are designed based on the system identification examination results. The vibration suppression effects are evaluated from the step response experiments.

The step response result reveals that the vibration at startup and acceleration can be reduced by the phase stabilization controller because the motor angular velocity in the frequency range around the resonant frequency is greatly suppressed. Our future works are the detail modeling of the driving unit including the bushes and the evaluation of the vibration suppression effects on changes in slip rate. In addition, we will develop further phase stabilized controller based on the Nyquist plot in the future.



Fig. 13. The step responses of $\omega_\mathrm{m}$.

# References

( 1 ) Y. Hori, "Future Vehicle Driven by Electricity and Control Research on Four-Wheel-Motored 〝UOT Electric March II〞", *IEEE Trans. on Industrial Electronics*, vol. 51, no. 5, pp. 954–962, 2004.

( 2 ) G. Mühlberg, W. Hackmann, and K. Buzziol, "Highly Integrated Electric Powertrain", *ATZ Elektron Worldwide*, vol. 12, pp. 42-45, 2017.

( 3 ) M. Martino, P. Pescetto, and G. Pellegrino "Advanced Functionally Integrated E-Axle for A-Segment Electric Vehicles", *2020 AEIT International Conference of Electrical and Electronic Technologies for Automotive*, pp. 1-6, 2020.

( 4 ) H. Fuse, H. Fujimoto, K. Sawase, N. Takahashi, R. Takahashi, Y. Okamura, and R. Koga, "Derivation of Dynamic Model of Two-Input-Two-Output Torque Difference Amplification Motor Drive System and Independent Left-and-Right Wheel Control with Decoupling Compensator", *IEEJ Journal of Industry Applications*, vol. 11, no. 3, pp. 427-436, 2022.

( 5 ) Y. Hosomi, S. Yamada, B. Nguyen, S. Nagai, and H. Fujimoto, "Basic Study on Energy-optimized Speed Trajectory for Electric Vehicles between Traffic Signals Based on Stochastic Model Using Low Frequency Floating Car Data", *The 9th IEEJ Int. Work. on Sensing, Actuation, Motion Control., Optim., Nanjing*, 2023.

( 6 ) S. Hazra and I. Pathak, "Engine mount design technique to address vehicle level Buzz, Squeak and Rattle", *2017 IEEE Transportation Electrification Conference*, pp. 1-5, 2017.

( 7 ) H. Fujimoto, J. Amada, and K. Maeda, "Review of Traction and Braking Control for Electric Vehicle", *Proc. the 8th IEEE Vehicle Power and Propulsion Conference*, pp. 1292-1299, 2012.

( 8 ) H. Chu, W. Shi, Y. Jiang, and B. Gao, "Driveline Oscillation Damping for Hybrid Electric Vehicles Using Extended-State-Observer-Based Compensator", *Sustainability*, vol. 15, no. 10, pp. 1-16, 2023.

( 9 ) N. Mizushima, S. Sato, H. Yagi, and H. Suzuki, "Improvement of Transient Operation Controllability in Engine Test Bench for Heavy-Duty Vehicles", *International Journal of Automotive Technology*, vol. 20, no. 6, pp. 1255-1262, 2019.

(10) H. Fujimoto, H. Yoshida, D. Kawano, Y. Goto, M. Tsuchimoto, and K. Sato, "Bench Test of Range Extension Autonomous Driving for Electric Vehicles Based on Optimization of Velocity Profile Considering Traffic Signal Information", *International Electric Vehicle Technology Conference and Automotive Power Electronics Japan*, 2016.

(11) M. Yoshimura and H. Fujimoto, "Driving Torque Control Method for Electric Vehicle with In-Wheel Motors", *Electrical Engineering in Japan*, vol. 181, no. 3, pp. 49-58, 2012.

(12) H. Fuse and H. Fujimoto, "Driving force controller considering lateral slip based on brush model for traction control of independent‐four‐wheel‐drive electric vehicle", *Electrical Engineering in Japan*, vol. 214, no. 1, pp. 52-61, 2020.

(13) H. Kuwahara and T. Murakami, "Tracked Vehicle Velocity Estimation by Disturbance Observer and Machine Learning, and its Application to Driving Force Control for Slippage Suppression", *IEEJ Journal of Industry Applications*, vo. 11, no. 1, pp. 69-75, 2022.

(14) K. Shirota, F. Baba, M. Horikoshi, and K. Sato, "Development of 〝Virtual and Real Simulator〞for Engine" *SAE Paper*, 2001-01-1355, 2001.

(15) ISO Standard 2631-1, "Mechanical vibration and shock -Evaluation of human exposure to whole-body vibration-", part 1. 1997.

(16) M. Kobayashi, S. Nakagawa, T. Atsumi, and T. Yamaguchi, "High-Bandwidth Servo Control Designs for Magnetic Disk Drives", *Proc. IEEE/ASME Int. Conf. Adv. Intell. Mechatron.*, pp. 1124-1129, 2001.
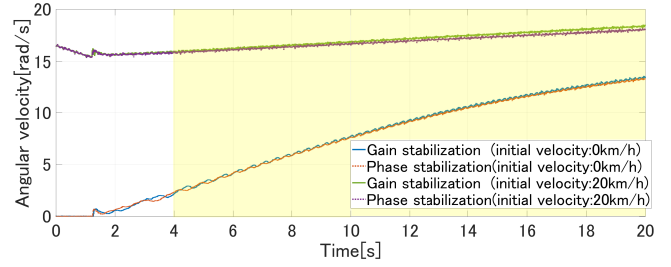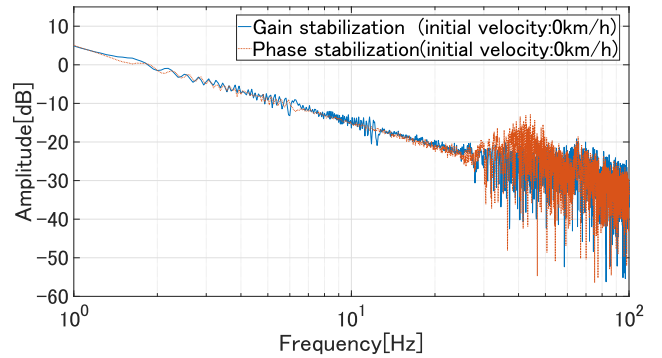
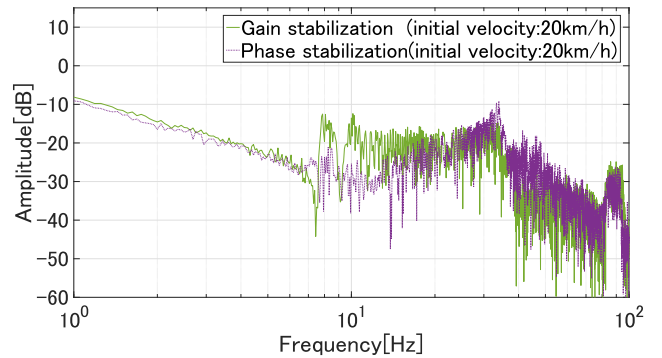Fig. 14. The frequency characteristics of $\omega_\mathrm{m}$ (the initial vehicle velocity: 0 km/h).



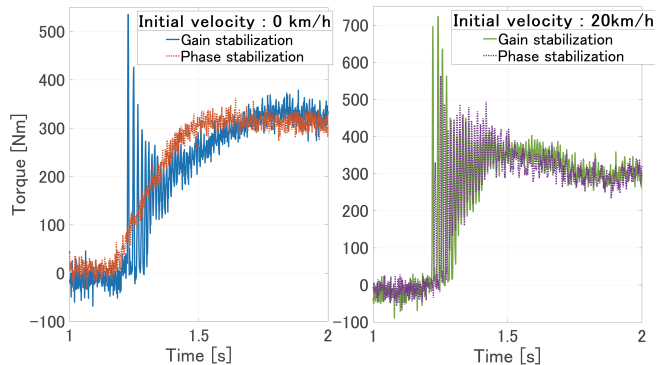Fig. 15. The frequency characteristics of $\omega_\mathrm{m}$ (the initial vehicle velocity: 20 km/h).



Fig. 16. The step responses of $T_\mathrm{s}$ (enlarged).